2021-03

Valence-induced effects on the electrical properties of NiMn2O4 ceramics with different Ni sources

Wu, Yiquan

Guan, F., Wu, Y., Milisavljevic, I., Cheng, X. and Huang, S. (2021), Valence-induced effects on the electrical properties of NiMn2O4 ceramics with different Ni sources. J Am Ceram Soc, 104: 5148-5156. https://doi.org/10.1111/jace.17760

Wiley

https://doi.org/10.1111/jace.17760

MISS FANG GUAN (Orcid ID : 0000-0002-0916-5958)

DR YIQUAN WU (Orcid ID : 0000-0001-8742-716X)

Article type : Article

Valence-induced effects on the electrical properties of $NiMn_2O_4$ ceramics with different Ni sources

Fang Guan,[1,2] Yiquan Wu,[2] Iva Milisavljevic, [2] Xin Cheng,[1] * Shifeng Huang, [1] *

[1] Shandong Provincial Key Laboratory of Preparation and Measurement of Building Materials, University of Jinan, Jinan, 250022, PR China

[2] Kazuo Inamori School of Engineering New York State College of Ceramics Alfred University, Alfred, NY 14802, USA

* Corresponding author

E-mail: ujn_chengxin@163.com; mse_huangsf@ujn.edu.cn

Abstract: Spinel-structured $NiMn_2O_4$ ceramics, with different valence Ni sources, were originally prepared using Ni_2O_3 and NiO as raw materials, and the effects of different valence Ni sources on their electrical properties were first investigated. XRD patterns show that both Ni_2O_3-based and NiO-based $NiMn_2O_4$ ceramics are single cubic spinel structures. SEM/EDS images indicate that the $NiMn_2O_4$ ceramics exhibited high density at the experiment-determined sintering temperatures. XPS results and Raman drifts prove that the Ni valence-induced changes of Mn ions at B-sites played a significant role in the electrical properties and thermal stability of $NiMn_2O_4$ ceramics. Compared with NiO-based $NiMn_2O_4$, the resistivity at 25 °C ($\rho_{25°C}$) of Ni_2O_3-based $NiMn_2O_4$ increased dramatically from 3109 Ω•cm to 106958 Ω•cm, the thermal constant ($B_{25/50}$) increased from 3264 K to 4473 K, and the resistance shifts after annealing for 1000 h at 150 °C decreased from 0.80% to 0.74%. The investigation of the relationship between the material properties and

This article has been accepted for publication and undergone full peer review but has not been through the copyediting, typesetting, pagination and proofreading process, which may lead to differences between this version and the Version of Record. Please cite this article as doi: 10.1111/JACE.17760

valence of Ni sources has provided a new and effective way for designing the spinel-structured negative temperature coefficient (NTC) materials by modulating the valence of ions at A-sites in the raw materials.

Keywords: $NiMn_2O_4$; NiO; Ni_2O_3; Electrical properties; Solid-state reaction

1. Introduction

Manganese-based spinel oxide ceramics have attracted substantial research interest in the field of NTC thermistors over the past few decades. They have been widely used for accurate temperature measurement and control in various domestic and industrial applications owing to their high sensitivity to temperature change, fast response, and low cost [1-5]. In general, they have a molecular formula AB_2O_4, in which A (generally divalent cations) and B atoms (generally trivalent cations) usually occupy separately the tetrahedral (A-sites) and octahedral sites (B-sites), which are formed by the close-packed array of the oxygen ions. However, some spinel oxides may change their crystal structure into a mixed spinel structure, that is, atoms A and B can occupy both octahedral and tetrahedral sites in the structure with a general formula of $(A_{1-x}B_x)[A_xB_{2-x}]O_4$ [6,7]. Among them, $NiMn_2O_4$ is one of the most commonly used NTC thermistors, known for its typical mixed spinel structure influenced by the Ni^{2+} ions. Specifically, the high octahedral preference of the Ni^{2+} ions produces a cubic structure with a general ion composition of $(Ni^{2+}_{1-x}Mn^{2+}_x)[Ni^{2+}_xMn^{3+}_{2-2x}Mn^{4+}_x]O_4$ [8]. On the other hand, this process can also affect the Jahn-Teller effect of Mn^{3+} ions at B-sites, which has been credited as the main reason for the electrical properties of manganese-based oxides [9].

Actually, the electrical properties and the crystal structure of NTC thermistors are closely related. Their resistances are strongly influenced by the cation distribution in the crystal structure [10]. In most of the earlier reports, the conducting behavior of the manganese-based spinel ceramics has been explained with the simple hopping mechanism taking place between the Mn^{3+} and Mn^{4+} ions located at the B-sites in the spinel structure, which is induced by the lattice vibrations [11-14]. Therefore, extensive studies have been done to adjust the electrical properties of $NiMn_2O_4$ through doping with different elements, such as Co, Fe, Cu, or their combination at the B-sites, which can

directly change the concentration ratio between Mn^{3+} and Mn^{4+} [15-18]. However, few studies have been devoted to modifying the electrical properties of $NiMn_2O_4$ by tuning the ions at the A-sites according to the literature reports, especially in the raw materials used for the preparation of the $NiMn_2O_4$ spinel. In fact, the Ni ions at A-sites play an important role in the electrical properties of $NiMn_2O_4$ based on the structural features mentioned before. This inspired us to investigate the influence of different valence Ni sources on the electrical properties of $NiMn_2O_4$. To the best of our knowledge, NiO has been used as the most common Ni source due to its valence state (Ni^{2+}), which is the preferred valence for the A-sites. In this work, Ni_2O_3 with a higher valence state of Ni^{3+} was selected as the new Ni source, while NiO was simultaneously employed to provide a comparison. An important relationship between the Ni sources and electrical properties and the main parameters (specific resistivity ρ, thermal constant B, and the resistance shift $\Delta R/R_0$) had been attempted to be established in the current research. Moreover, the synthesis conditions and sintering method also have a direct influence on the microstructure of the $NiMn_2O_4$ ceramics and consequently on the electrical performance of the material. In general, the smaller the grain size, the stronger and denser is the ceramic material, which can contribute to its high thermal stability [19]. Therefore, the traditional solid-state reaction and two-step sintering (TSS) methods were used to obtain pure-phase ceramics with small grain size because there is a temperature range during the TSS, known as the "kinetic window", in which densification can occur without concurrent grain growth [20-23]. We hope that this work can provide a new perspective on the compositional and structural design of the spinel NTC materials.

2. Experimental Procedure

The single-spinel phase $NiMn_2O_4$ powder samples from different Ni sources were synthesized using the traditional solid-state reaction method. Stoichiometric amounts of Mn_2O_3 (99.99%, Aladdin) and different Ni sources with different valence states of Ni, i. e. Ni_2O_3 (99.00%, Macklin) and NiO (99.00%, Aladdin) were used as the raw materials. The weighed powders and ethanol (1:1 mass ratio) were ball-milled for 15 h in an agate jar using agate balls as milling media. The obtained slurries were dried at 80 °C in an oven for 12 h. The two dried powders were ground and

then calcined at 900 °C (Ni_2O_3-based) and 950 °C (NiO-based) for 2 h, then ball-milled again for 10 h and dried. The obtained single-spinel phase $NiMn_2O_4$ powders were granulated with an organic binder (PVA420, PVOH Kuraray, Japan) and uniaxially pressed at 10 MPa, followed by the cold isostatic pressing at 350 MPa, to form disk-shaped powder compacts with a diameter of 10 mm and thickness of 2 mm. The pressed green bodies were then sintered by the TSS approach in air atmosphere. The Ni_2O_3-based samples were heated at a low rate of 1 °C/min to 600 °C and kept at that temperature for 2 h to remove the PVA binder. After that, the samples were heated to the first-step sintering temperature of 1280 °C at a rate of 20 °C/min, held for 15 minutes, and then the temperature was ramped down in 3 min to the second-step sintering temperature of 1130 °C, followed by a 15-hour dwell. After the sintering was finished, the samples were fast cooled down to room temperature. In the case of the NiO-based samples, the first-step sintering temperature and the second-step sintering temperature were 1300 °C and 1150 °C, respectively.

The thermo-gravimetric (TG) analysis and differential scanning calorimetry (DSC) of the precursor powders were conducted using a synchronous thermal analyzer (STA449F3, Netzsch, Selb, Germany) to determine the calcination temperature of the $NiMn_2O_4$ powders. To obtain the sintering temperature of the $NiMn_2O_4$ ceramics, the densification behaviors were studied with a dilatometer (Netzsch DIL 402C, Selb, Germany). The particle size of the powder samples was tested by a laser particle sizer (LS13320, Beckman Coulter, America). The structural properties were analyzed by an X-ray diffractometer (XRD: BRUKER D8-ADVANCE, Germany) with Cu Kα radiation (λ=1.5406Å). The microstructure was examined by a scanning electron microscope (SEM: HITACHI S-2500, Japan) coupled with the OXFORD INCA200 energy-dispersive X-ray spectrometer (EDS). The valence states of cations were characterized by the X-ray photoelectron spectroscopy (XPS: Thermo Fisher Scientific ESCALAB XI, America) with Al Ka radiation (hm=1486.6 eV). To measure the electrical resistance, the sintered ceramic samples were first coated with silver paste, annealed at 850 °C for 30 min, and then attached to silver wires as the electrode leads. Electrical resistance was measured in the temperature range from -100 °C to 150 °C by a four-probe technique using an Agilent 34401A digital multimeter. The aging tests were conducted by keeping the sintered samples in an oven at 150 °C in the air for 1000 h.

3. Results and discussion

Figure 1 presents the TG/DSC curves of the Ni_2O_3-based and NiO-based $NiMn_2O_4$ powders mixed with PVA under air atmosphere, obtained in the temperature range from room temperature to 1000 °C, and their particle size distributions. From Figure 1(a) and Figure 1(c), it can be seen that the Ni_2O_3-based and NiO-based $NiMn_2O_4$ powders displayed a similar trend of TG and DSC curves. There were generally three stages of weight loss. The first stage occurred from room temperature to about 210 °C, with a weight loss of about 2.0%, which was associated with the evaporation of the absorbed water and the removal of the crystallized water [24], accompanied by an endothermic peak between 150 °C and 230 °C. The second stage, associated with the burnout of the organic PVA binder, happened in the 540-640 °C range and was accompanied by a strong exothermic peak centered at 600 °C. The third stage took place in the range between 780 °C and 910 °C (Ni_2O_3-based) and 890 °C and 950 °C (NiO-based), accompanied by an exothermic peak centered at 826 °C (Ni_2O_3-based) and 900 °C (NiO-based) in the DSC curve; this weight loss may correspond to the oxygen loss during the formation process of the spinel structure [25]. There was no significant weight loss and change above 900 °C (Ni_2O_3-based) and 950 °C (NiO-based), which indicated the complete formation of $NiMn_2O_4$ spinel structure with cations redistribution. Thus, 900 °C and 950 °C were set as the calcination temperatures of Ni_2O_3-based and NiO-based $NiMn_2O_4$ powders, respectively. The reason for a somewhat lower calcination temperature of Ni_2O_3-based $NiMn_2O_4$ may be the reduction reaction of Ni_2O_3 from Ni^{3+} to Ni^{2+} before the $NiMn_2O_4$ spinel formation. This reduction reaction is an exothermic process that can induce the crystallization process to proceed earlier than that of NiO-based $NiMn_2O_4$ [26]. The calcined $NiMn_2O_4$ powders exhibited uniform and small particle size with a Gaussian distribution, as shown in Figure 1(b) and Figure 1(d), which are the critical factors of the densification during the sintering process. Moreover, the lower calcination temperature of Ni_2O_3-based $NiMn_2O_4$ produced particles that were smaller in size compared with NiO-based $NiMn_2O_4$.

Figure 2 shows the XRD patterns of the Ni_2O_3-based and NiO-based $NiMn_2O_4$ powders calcined at 900 °C and 950 °C, respectively. The two samples exhibited a single cubic spinel phase

$NiMn_2O_4$ (JCPDS: 01-1110) without any other impurity phases being detected, which indicated that the Ni ions from Ni_2O_3 entered completely the A-sites of the $NiMn_2O_4$ spinel and thereby demonstrated the same occupying behavior as the Ni ions from NiO. However, a slight peak shift to higher angles of Ni_2O_3-based $NiMn_2O_4$ compared with the NiO-based $NiMn_2O_4$ samples can be observed in Figure 2(b), which was more obvious in Figure 2(a), an enlarged detail in the 2θ range from 32 ° to 40 °. This means that the Ni_2O_3-based $NiMn_2O_4$ exhibited a lattice constriction compared with the NiO-based $NiMn_2O_4$. This difference could result from the different valence states of Ni sources and also the Jahn-Teller effect of Mn^{3+}, which is common in manganese-based spinel materials [27]. In Ni_2O_3, Ni was present in Ni^{3+} valence state, however, in the presence of Mn_2O_3, to form $NiMn_2O_4$, Ni^{3+} ions have to convert into Ni^{2+} ions. On the other hand, to maintain the electrical neutrality, Mn^{3+} ions, the most common form of Mn in $NiMn_2O_4$ [28], tend to convert into Mn^{4+}, which will be further confirmed by the XPS analysis. As a result, a decrease of the lattice parameter occurs because the ionic radius of Mn^{4+} (0.053 nm) is smaller than that of Mn^{3+} (0.0645 nm) for occupying the octahedral sites of the $NiMn_2O_4$ spinel structure.

The dilatometer curves of Ni_2O_3-based and NiO-based $NiMn_2O_4$ compacts are presented in Figure 3. It can be seen that their maximum shrinkages were at 1225 °C and 1245 °C, respectively, and the maximum shrinkage values were almost the same -7.24%. Therefore, 1225 °C and 1245 °C can be considered as their conventional sintering temperatures. Based on these results, slightly higher temperatures (~50 °C) than the conventional sintering temperatures, 1280 °C and 1300 °C, were set as the first-step sintering temperatures of Ni_2O_3-based and NiO-based $NiMn_2O_4$, respectively, to help overcome the high activation energies for the matter migration or diffusion. As their second-step sintering temperatures, 1130 °C and 1150 °C were chosen, respectively, which were relatively below (~100 °C) the conventional sintering temperature, allowing for the densification to proceed without a significant grain growth occurring at the same time [29,30]. The lower sintering temperature for Ni_2O_3-based $NiMn_2O_4$ resulted from its smaller particle size, which produced a larger specific surface area and provided a larger contact area between the reactants [31].

Figure 4 presents the SEM images and EDS maps of the sintered Ni_2O_3-based and NiO-based $NiMn_2O_4$ samples. Both samples exhibited dense microstructure with small grain size varying from approximately 0.5 μm to 2.5 μm. Moreover, the EDS maps presented a uniform elemental distribution with no significant difference in the element content. All the results proved that the different valence states of Ni had no obvious effect on the microstructure and element distribution in spinel $NiMn_2O_4$. However, the content ratios of Ni/Mn for Ni_2O_3-based and NiO-based $NiMn_2O_4$ ceramics were 24.98/46.89 and 24.11/46.34, respectively, which were similar to each other and a little higher than that in the formula of $NiMn_2O_4$, 1/2. This mild non-stoichiometric phenomenon should be caused by the volatilization of Mn. It is easier for Mn to volatilize than Ni because Mn has a lower melting point (1244 °C) which is also much lower than the sintering temperature in the first step. Zheng, et al. have confirmed that the volatilization of Mn in Cu-Al-Mn alloy can be enhanced by increasing the time of heat treatment and the treatment temperature, and the electrical resistance and hardness of the alloy can be adjusted by controlling the volatilization amount of Mn [32].

Figure 5 presents the electrical properties of $NiMn_2O_4$ ceramics with different Ni sources. Figure 5(a) and Figure 5(b) manifest that the resistivities decreased exponentially with the increasing temperature, indicating that the prepared $NiMn_2O_4$ ceramics exhibited typical NTC characteristics. Moreover, the relationships between $\ln\rho$ and $1/T$ appeared perfectly linear, demonstrating that the resistivities obey the well-known Arrhenius relation: $\rho=\rho_0\exp(B/T)$, from which the thermal constant B can be determined. B is also generally obtained from the relation $B=E_a/k$, where E_a is the activation energy and k the Boltzmann constant. The calculated $B_{25/50}$ values, E_a, ρ_{25}, and ρ_{50} of Ni_2O_3-based and NiO-based $NiMn_2O_4$ ceramics are listed in Table 1. By contrast, Ni from Ni_2O_3 can significantly increase the resistivities of $NiMn_2O_4$ by two orders of magnitude and improve the $B_{25/50}$ value by a certain amount. Such a dramatic increase of resistivity may be attributed to the valence-induced changes in the conduction mechanism by different valence Ni sources. It is believed that hopping conduction is the main conduction mechanism in the manganese-based NTC thermistors [33,34]. In $NiMn_2O_4$ thermistors, e_g-electrons with higher energy in Mn^{3+} jump into the empty e_g-orbitals of Mn^{4+}, and Mn ions change valence to produce hopping conduction. As

explained earlier, when Ni_2O_3 was used as the Ni source, the reduction process of Ni ions from Ni^{3+} to Ni^{2+} promoted the conversion of Mn^{3+} to Mn^{4+}, resulting in the consumption of Mn^{3+}. This process subsequently reduced the Mn^{3+} content that participated in the hopping conduction and also weakened the Jahn-Teller effect of Mn^{3+} ions, thereby increasing the resistivity. Further investigation of the thermal stability demonstrated that Ni_2O_3 could also reduce the aging coefficient of the $NiMn_2O_4$ ceramics (observed in Figure 5(c)), contributed by the Ni^{3+}-induced decrease of Mn^{3+}. Less Mn^{3+} in the system provided not only less variable valence ion pairs (Mn^{2+}/Mn^{3+} or Mn^{3+}/Mn^{4+}) but also weakened the Jahn-Teller effect of Mn^{3+} ions [35]. The high thermal stability with the resistance shifts less than 0.80% enables this material to have potential practical application.

Moreover, the XPS analysis was also carried out to investigate the differences in the electrical properties of $NiMn_2O_4$ with different Ni sources. Figure 6 displays the XPS spectra of Ni_2O_3-based and NiO-based $NiMn_2O_4$ samples. Figure 6(a) and Figure 6(b) present the XPS wide-scan spectra of Mn2p and Ni2p for the two samples. It can be seen that no obvious shift of Ni2p peaks could be observed, while a distinct shift of Mn2p peaks from low binding energy to higher occurred between the two samples. For example, the $Mn2p_{3/2}$ peak shifted from 641.3 eV in NiO-based $NiMn_2O_4$ to 641.8 eV in Ni_2O_3-based $NiMn_2O_4$. This indicated that the valence state of Ni ions in both samples was similar to each other, while that of Mn ions was in a higher valence-state in the Ni_2O_3-based $NiMn_2O_4$ [36]. In addition, the $Ni2p_{3/2}$ peak contained two components: Ni^{2+}, Ni^{3+} [37,38] as shown in Figure 6(c) and 6(e), and the $Mn2p_{3/2}$ peak contained three components: Mn^{2+}, Mn^{3+}, and Mn^{4+} [27], as shown in Figure 6(d) and 6(f), that were resolved by the curve fitting of the $Ni2p_{3/2}$ and $Mn2p_{3/2}$ lines.

The concentration of each component was also obtained from the XPS results and listed in Table 2. It was found that the concentrations of Ni ions in the two samples were also similar to each other. And the Mn^{3+} ions were the main ions in the NiO-based $NiMn_2O_4$, which is in agreement with the previous studies [28,39], whereas Mn^{4+} was the dominant ion form of Mn for Ni_2O_3-based $NiMn_2O_4$. This significant change from Mn^{3+} in NiO-based $NiMn_2O_4$ to Mn^{4+} in Ni_2O_3-based $NiMn_2O_4$ was

consistent with the previous XRD analysis and should be caused by the different valence Ni sources. The similar valence states and concentrations of Ni ions in both samples synthesized by different Ni sources with totally different valence states demonstrated that there should be a opposite process happened in the two samples, that was the $Ni^{2+} \rightarrow Ni^{3+}$ process in NiO-based $NiMn_2O_4$ and the $Ni^{3+} \rightarrow Ni^{2+}$ process in Ni_2O_3-based $NiMn_2O_4$. Then the process of $Mn^{4+} \rightarrow Mn^{3+}$ in NiO-based $NiMn_2O_4$ and the process of $Mn^{3+} \rightarrow Mn^{4+}$ in Ni_2O_3-based $NiMn_2O_4$ were promoted to maintain the electrical neutrality, resulting in the increase of Mn^{3+} and Mn^{4+} in NiO-based $NiMn_2O_4$ and Ni_2O_3-based $NiMn_2O_4$, respectively. Therefore, we speculate that the valence-induced difference of Mn ions by different Ni sources, especially Mn^{3+} (the Jahn-Teller ions) concentration, should be directly responsible for the variation in the electrical properties of $NiMn_2O_4$ as discussed earlier in the electrical properties. Besides, the mixed-states of Ni and Mn ions, Ni^{2+}/Ni^{3+} and $Mn^{2+}/Mn^{3+}/Mn^{4+}$, created the possibility that some of Ni ions could occupy the B-sites of the spinel structure and then formed a possible ion composition of $(Ni^{2+}_{1-a-b}Mn^{2+}_{d})_{tet}[Ni^{2+}_{a}Ni^{3+}_{b}Mn^{3+}_{y-c-d}Mn^{4+}_{c}]_{oct}O_4$ [8,37]. Moreover, the volatilization of Mn discussed in the EDS analysis could also enhance the occupation of Ni ions at B-sites.

To further investigate the influence of different Ni sources on the electrical properties of $NiMn_2O_4$ by changing the concentration of different valence-state Mn ions, Raman analysis was carried out to study the electronic structure of Mn ions and the spinel structure distortion. Previous studies have demonstrated that Raman spectra can be an effective way to study the electronic structure of transition metal ions [40,41]. The Raman spectra of $NiMn_2O_4$ samples with different Ni sources are presented in Figure 7. The strongest signals for NiO-based and Ni_2O_3-based $NiMn_2O_4$, centered at 622.2 cm^{-1} and 624.2 cm^{-1}, respectively, should be attributed to Mn-O stretching vibration of the $[MnO_6]$ octahedron [42,43]. Moreover, the Mn-O stretching vibration in Ni_2O_3-based $NiMn_2O_4$ had been found to shift to the higher wavenumber (blueshift) when compared with that in NiO-based $NiMn_2O_4$, indicating an increase in frequency and bond energy of the Mn-O stretching vibration of $[MnO_6]$ octahedral for Ni_2O_3-based $NiMn_2O_4$ [44]. Furthermore, this also indicated that the Mn-O group had been distorted, which could be due to the decrease in ion radius of Mn^{4+}

compared with Mn^{3+}. Thus, it should be the deformation of [MnO_6] octahedron, induced indirectly by the different Ni sources, that generated the change in electrical properties [45]. This deformation of the [MnO_6] octahedron could further inhibit the electron hopping to some extent resulting in high resistivity and stability behavior [28].

4. Conclusions

The spinel-type $NiMn_2O_4$ ceramics with different valence Ni sources were originally synthesized by the solid-state reaction and TSS method, using NiO and Ni_2O_3 oxides as different valence Ni sources. The effects of different valence Ni sources on the electrical properties of $NiMn_2O_4$ ceramics were investigated. Results show that the Ni_2O_3 can significantly increase the resistivity of $NiMn_2O_4$ and improve the B value and thermal stability at the same time. The $\rho_{25°C}$, $B_{25/50}$ value, and resistance shifts ($\Delta R/R_0$) after aging for 1000 h at 150 °C were 106958 Ω•cm and 3109 Ω•cm, 4473 K and 3264 K, and 0.74% and 0.80% for Ni_2O_3-based and NiO-based $NiMn_2O_4$, respectively. Moreover, the action mechanism of different valence Ni sources on the electrical properties of $NiMn_2O_4$ was realized indirectly by changing the concentration of different valence-stated Mn ions at B-sites. This work demonstrates that the change of the Ni sources at A-sites can be an effective and simple way to adjust the electrical properties of $NiMn_2O_4$ ceramics, which can provide a new pathway to the design of spinel NTC materials.

Acknowledgement

The work was supported by the National Natural Science Foundation of China (Grant No. 51632003, Grant No. 51671094, and Grant No. 5176145023), the Taishan Scholars Program, Case-by-Case Project for Top Outstanding Talents of Jinan, the National Key Research and Development Program of China (Grant No. 2016YFB0303505).

References

1. Gillot B, Baudour JL, Bouree F, Metz R, Legros R, Rousset A. Ionic configuration and cation distribution in cubic nickel manganite spinels $Ni_xMn_{3-x}0_4$ ($0.57<x<1$) in relation with thermal histories. Solid-state Ionics. 1992;58:155-161.
2. Schubert M, Münch C, Schuurman S, Poulain V, Kita J, Moos R. Characterization of nickel

manganite NTC thermistor films prepared by aerosol deposition at room temperature. J. Eur. Ceram. Soc. 2018;38(2):613-619.

3. Ren W, Zhang YC, Zhu NN, Feng AL, Shang SG. Synthesis of $NiMn_2O_4$ thin films via a simple solid-state reaction route. Ceram. Int. 2020;46:11675-11679.
4. Song J, Li B, Chen Y, et al. A high-performance Li-Mn-O Li-rich cathode material with Rhombohedral symmetry via Intralayer Li/Mn disordering. Adv. Mater. 2020;32(16). Available from: https://doi:10.1002/adma.202000190.
5. Wei L, Tao J, Yang Y, et al. Surface sulfidization of spinel $LiNi_{0.5}Mn_{1.5}O_4$ cathode material for enhanced electrochemical performance in lithium-ion batteries. Chem. Eng. J. 2020;384. Available from: https://doi.org/10.1016/j.cej.2019.123268.
6. Sickafus KE, Wills JM, Grimes NW. Structure of spinel. J. Am. Ceram. Soc. 1999;82(12):3279-3292.
7. Park K. Fabrication and electrical properties of Mn-Ni-Co-Cu-Si oxides negative temperature coefficient thermistors. J. Am. Ceram. Soc. 2005;88(4):862-866.
8. Schmidt R, Basu A, Brinkman AW. Small polaron hopping in spinel manganates, Phys. Rev. B. 2005;72(11). Available from: https://doi.org/10.1103/PhysRevB.72.115101.
9. Konarov A, Jo JH, Choi JU, et al. Exceptionally highly stable cycling performance and facile oxygen-redox of manganese-based cathode materials for rechargeable sodium batteries. Nano Energy. 2019;59:197-206.
10. Schmidt R, Basu A, Brinkman AW, Klusek Z, Datta PK. Electron-hopping modes in $NiMn_2O_{4+\delta}$ materials. Appl. Phys. Lett. 2005;86. Available from: https://doi.org/10.1063/1.1866643.
11. Feteira A. Negative temperature coefficient resistance (NTCR) ceramic thermistors: an industrial perspective. J. Am. Ceram. Soc. 2009;92(5):967-983.
12. Wei C, Feng Z, Scherer GG, Barber J, Shao-Horn Y, Xu ZJ. Cations in octahedral sites: a descriptor for oxygen electrocatalysis on transition-metal spinels. Adv. Mater. 2017;29(23). 1606800, Available from: https://doi:10.1002/adma.201606800.
13. Kanade SA, Puri V. Electrical properties of thick-film NTC thermistor composed of

$Ni_{0.8}Co_{0.2}Mn_2O_4$ ceramic: effect of inorganic oxide binder. Mater. Res. Bull. 2008;43:819-824.
14. Savic SM, Nikolic MV, Aleksic OS, Slankamenac M, Zivanov M, Nikolic PM. Intrinsic resistivity of sintered nickel manganite vs. powder activation time and density. Sci. Sin. 2008;40:27-32.
15. Wang W, Liu X, Gao F, Tian C. Synthesis of nanocrystalline $NiCo_{0.2}Mn_{1.8}O_4$ powders for NTC thermistor by a gel auto-combustion process. Ceram. Int. 2007;33(3):459-462.
16. Varghese JM, Seema A, Dayas KR. Microstructural electrical and reliability aspects of chromium doped Ni-Mn-Fe-O NTC thermistor materials. Mater. Sci. Eng. B. 2008;149(1):47-52.
17. Kanade SA, Puri V. Properties of thick film $Ni_{0.6}Co_{0.4}Fe_yMn_{2-y}O_4$: ($0 \leq y \leq 0.5$) NTC ceramic. J. Alloys Compd. 2009;475(1-2):352-355.
18. Muralidharan MN, Rohini PR, Sunny EK, Dayas KR, Seema A. Effect of Cu and Fe addition on electrical properties of Ni-Mn-Co-O NTC thermistor compositions. Ceram. Int. 2012;38(8):6481-6486.
19. Wang SW, Zhang LB, Yang Z, et al. Two-step co-sintering method to fabricate anode-supported $Ba_3Ca_{1.18}Nb_{1.82}O_{9-\delta}$ proton-conducting solid oxide fuel cells. J. power sources. 2012;215:221-226.
20. Wang XH, Chen PL, Chen IW. Two-Step Sintering of ceramics with constant grain-size, I. Y_2O_3. J. Am. Ceram. Soc. 2006;89(2):431-437.
21. Lóh NJ, Simão L, Faller CA, Jra ADN, Montedo ORK. A review of two-step sintering for ceramics. Ceram. Int. 2016;42(11):12556-12572.
22. Sutharsini U, Thanihaichelvan M, Singh R. Two-Step Sintering of Ceramics, in: I. Shishkovsky (Ed.), Sintering of Functional Materials, InTech. 2018. Available from: https://doi.org/10.5772/68083.
23. Ma CJ, Gao H. Preparation and characterization of single-phase $NiMn_2O_4$ NTC ceramics by two-step sintering method. J. Mater. Sci: Mater. Electron. 2017;28(9):6699-6703.
24. Yang J, Zhang HM, Sang X, Chang AM, Su Z. Study on ion migration characteristics and aging stability of $MgTiO_3$ and $LaTiO_3$ composites ceramic for high temperature negative

temperature coefficient ceramics. J Mater Sci: Mater Electron. 2020;31:7067-7075.
25. Chen L, Zhang QN, Yao JC, et al. Formation of Mn-Co-Ni-O nanoceramic microspheres using in situ ink-jet printing: sintering process effect on the microstructure and electrical properties. Small. 2016;12(36):5027-5033.
26. Yang M, Liu JX, Li SK, et al. Self-sustained solid-state exothermic reaction for scalable graphene production. Mater. Des. 2020;196. Available from: https://doi.org/10.1016/j.matdes.2020.109135.
27. Kong WW, Shi Q, Gao B, Chang AM. Improvement of electrical properties of single-phase film thermistors by a $Ni_{0.75}Mn_{2.25}O_4/LaMnO_3$ bilayer structure. J Mater Sci: Mater Electron. 2017;28(4):3837-3842.
28. Wang B, Yao JC, Wang JH, Chang AM. Valence-induced distortion controls the resistivity and thermal stability of $Co_{2.77}Mn_{1.71}Fe_{1.10}Zn_{0.42}O_8$ ceramics. Mater. Des. 2020;192. Available from: https://doi.org/10.1016/j.matdes.2020.108736.
29. Chen IW, Wang XH. Sintering dense nanocrystalline ceramics without final-stage grain growth. Nature. 2000;404(6774):168-171.
30. Mazaheri M, Zahedi AM, Sadrnezhaad SK. Two-Step sintering of nanocrystalline ZnO compacts: effect of temperature on densification and grain growth. J. Am. Ceram. Soc. 2008;91(1):56-63.
31. Campbell CT, Parker SC, Starr DE. The effect of size-dependent nanoparticle energetics on catalyst sintering. Science. 2002;298(5594):811-814.
32. Zheng YH, Liu CX, Liu WF, Li CJ. Volatilization of Mn in Cu-Al-Mn alloy during heat-treatment. Trans. Mater. Heat Treat. 2008;29(2):22-25.
33. Guan F, Dang ZW, Huang SF, et al. $LaCr_{1-x}Fe_xO_3$ ($0 \leq x \leq 0.7$): A novel NTC ceramic with high stability. J. Eur. Ceram. Soc. 2020;40(15):5597-5601.
34. Feterira A, Reichmann K. NTC ceramic: Past, Present and Future. Adv. Sci. Technol. 2010;67:124-133.
35. Schubert M, Münch C, Schuurman S, Poulain V, Kita J, Moos R. Thermal treatment of aerosol deposited $NiMn_2O_4$ NTC thermistors for improved aging stability. Sensors. 2018;18(11).

Available from: https://doi:10.3390/s18113982.
36. Zhang XB, Ren W, Kong WW, et al. Effect of sputtering power on structural, cationic distribution and optical properties of $Mn_2Zn_{0.25}Ni_{0.75}O_4$ thin films. Appl. Surf. Sci. 2018;435:815-821.
37. Gao FY, Tang XL, Sani Z, et al. Spinel-structured Mn-Ni nanosheets for NH_3-SCR of NO with good H_2O and SO_2 resistance at low temperature. Cat. Sci. Technol. 2020;22. Available from: DOI: 10.1039/D0CY01337D.
38. Kurilenko KA, Shlyakhtin OA, Brylev OA, Drozhzhin OA. The effect of synthesis conditions on the morphology, cation disorder and electrochemical performance of $Li_{1+x}Ni_{0.5}Mn_{0.5}O_2$. 2015;152:255-264.
39. Kumar SRS, Hedhili MN, Alshareef HN, Kasiviswanathan S. Correlation of Mn charge state with the electrical resistivity of Mn doped indium tin oxide thin films. Appl. Phys. Lett. 2010;97(11). Available from: https://doi:10.1063/1.3481800.
40. Granone LI, Ulpe AC, Robben L, et al. Effect of the degree of inversion on optical properties of spinel $ZnFe_2O_4$. Phys. Chem. Chem. Phys. 2018;20(44):28267-28278.
41. Wei Y, Kim KB, Chen G. Evolution of the local structure and electrochemical properties of spinel $LiNi_xMn_{2-x}O_4$ ($0 \le x \le 0.5$). Electrochim. Acta. 2006;51(16):3365-3373.
42. Tiwari P, Kumar S, Rath C. Probing structural transformation and optical and magnetic properties in Cr doped $GdMnO_3$: Jahn-Teller distortion, photoluminescence and magnetic switching effect. RSC Adv. 2019;9(68):39871-39882.
43. Julien C. Raman spectra of birnessite manganese dioxides. Solid State Ionics. 2003;159(3-4):345-356.
44. Jia H, Wang Z, Li C, et al. Designing oxygen bonding between reduced graphene oxide and multishelled Mn_3O_4 hollow spheres for enhanced performance of supercapacitors. J. Mater. Chem. A. 2019;7(12):6686-6694.
45. Bersuker IB. Modern aspects of the Jahn-teller effect theory and applications to molecular problems. Chem. Rev. 2001;101(4):1067-1114.

Figure and Table Caption List:

Figure 1. The TG/DSC curves (a) and particle size distribution (b) of Ni_2O_3-based $NiMn_2O_4$ calcined at 900 °C, and the TG/DSC curves (c) and particle size distribution (d) of NiO-based $NiMn_2O_4$ calcined at 950 °C.

Figure 2. a) XRD patterns of Ni_2O_3-based and NiO-based $NiMn_2O_4$ calcined powders and b) a partial enlarged detail of Fig. 2(a) from 2θ=32 ° to 40 °.

Figure 3. The thermodilatometric curves (shrinkage versus temperature) of Ni_2O_3-based and NiO-based $NiMn_2O_4$ compacts measured at a heating rate of 5 °C/min.

Figure 4. SEM images and EDS mapping of the sintered samples for the different valence of Ni: (a) Ni_2O_3-based $NiMn_2O_4$, and (b) NiO-based $NiMn_2O_4$.

Figure 5. Plots of the temperature dependence on resistivity in the temperature range from -100 °C to 150 °C for Ni_2O_3-based $NiMn_2O_4$ (a) and NiO-based $NiMn_2O_4$ ceramics (b) (the inset images represent the plots of the logarithm of the electrical resistivity (ln ρ) versus the reciprocal of the absolute temperature (1000/T)), and plots of $\Delta R/R_0$ and the aging time for Ni_2O_3-based $NiMn_2O_4$ and NiO-based $NiMn_2O_4$ ceramics (c) sintered via the two-step sintering approach.

Figure 6. XPS spectra of $NiMn_2O_4$ samples with different valence states of Ni sources: (a) the Ni2p spectra, (b) the Mn2p spectra, (c) $Ni2p_{3/2}$ spectra of NiO-based $NiMn_2O_4$, (d) $Mn2p_{3/2}$ spectra of NiO-based $NiMn_2O_4$, (e) $Ni2p_{3/2}$ spectra of Ni_2O_3-based $NiMn_2O_4$, and (f) $Mn2p_{3/2}$ spectra of Ni_2O_3-based $NiMn_2O_4$. All peaks have been calibrated with respect to the C1s peak at 284.6 eV.

Figure 7. Normalized Raman spectra of $NiMn_2O_4$ with different Ni sources.

Table 1. Resistivity at 25 °C and 50 °C, $B_{25/50}$ constant, and activation energy of $NiMn_2O_4$ ceramics with different Ni sources.

Table 2. The relative concentrations of Ni and Mn ions in $NiMn_2O_4$ with different Ni sources.

Tables:

Table 1

Ni source	ρ_{25} (Ω•cm)	ρ_{50} (Ω•cm)	$B_{25/50}$ (K)	Ea (eV)
Ni_2O_3	106958	33468	4473	0.618
NiO	3109	1331	3264	0.451

Table 2

Sample	Ni^{2+} (%)	Ni^{3+} (%)	Mn^{2+} (%)	Mn^{3+} (%)	Mn^{4+} (%)
NiO-based $NiMn_2O_4$	67.2	31.8	19.6	55.6	24.8
Ni_2O_3-based $NiMn_2O_4$	65.6	34.4	20.3	30.7	49.0

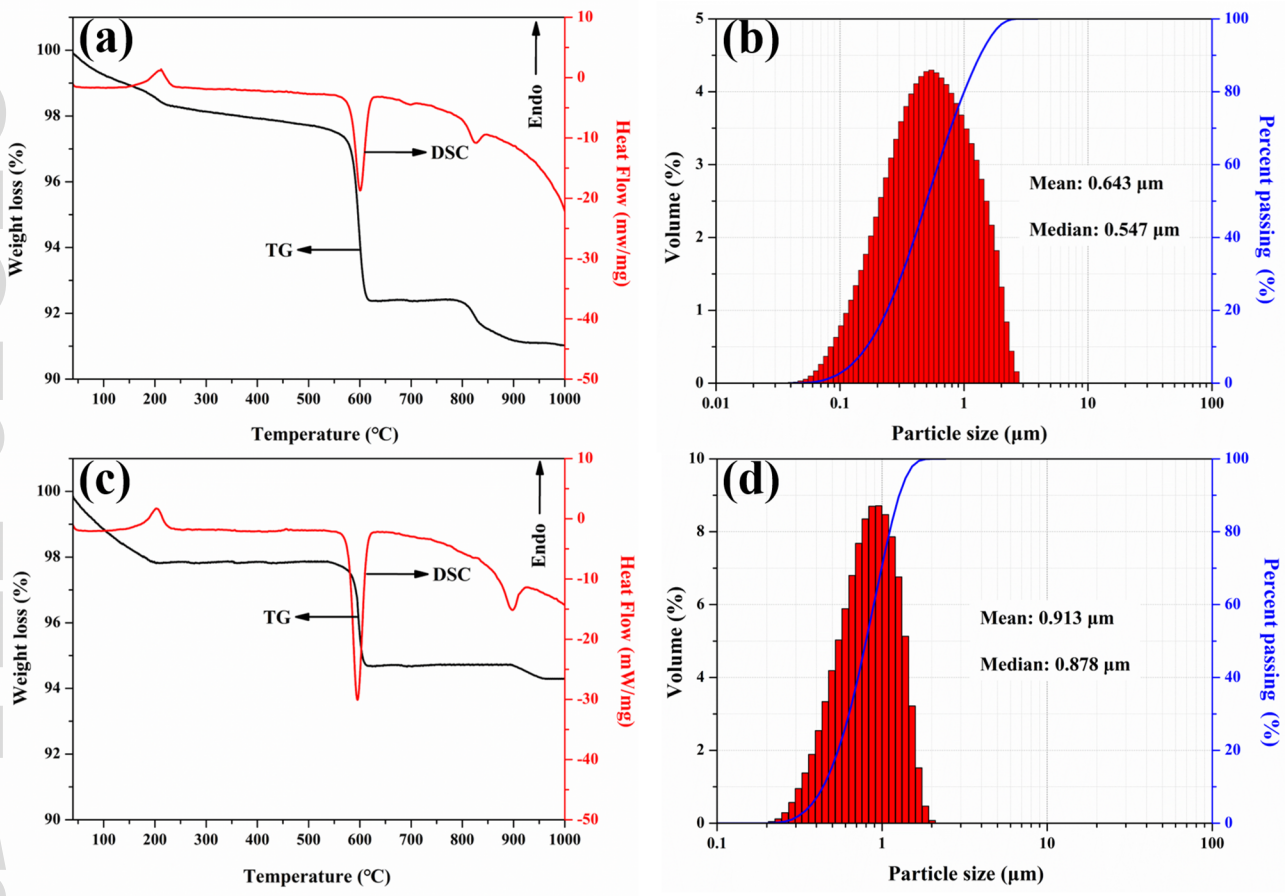

jace_17760_f1.tif

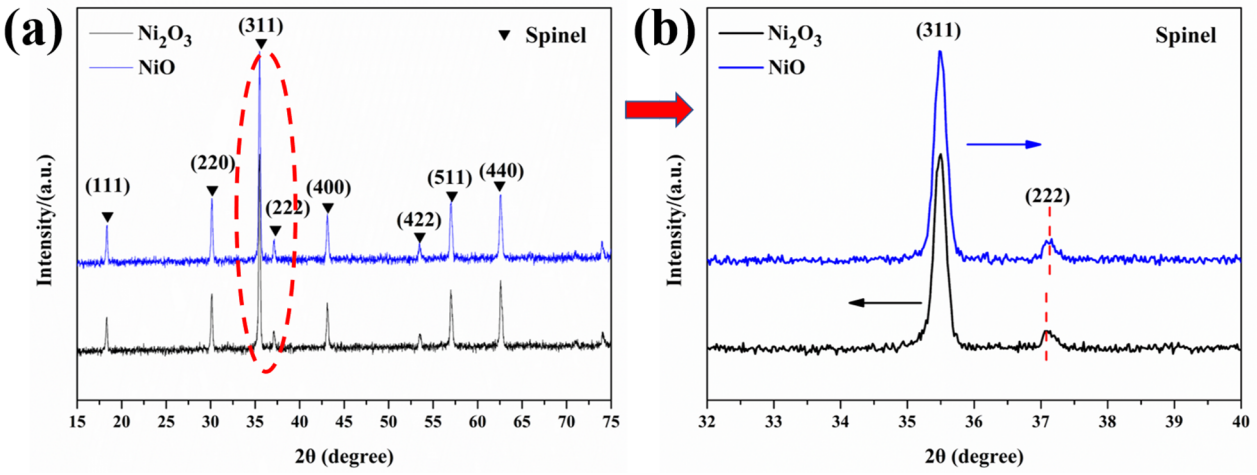

jace_17760_f2.tif

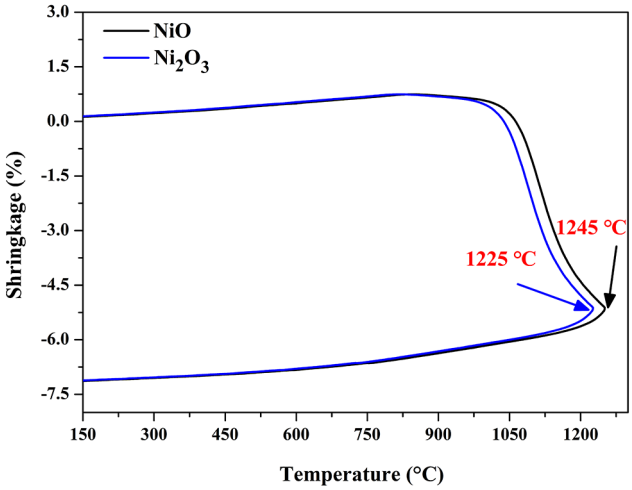

jace_17760_f3.tif

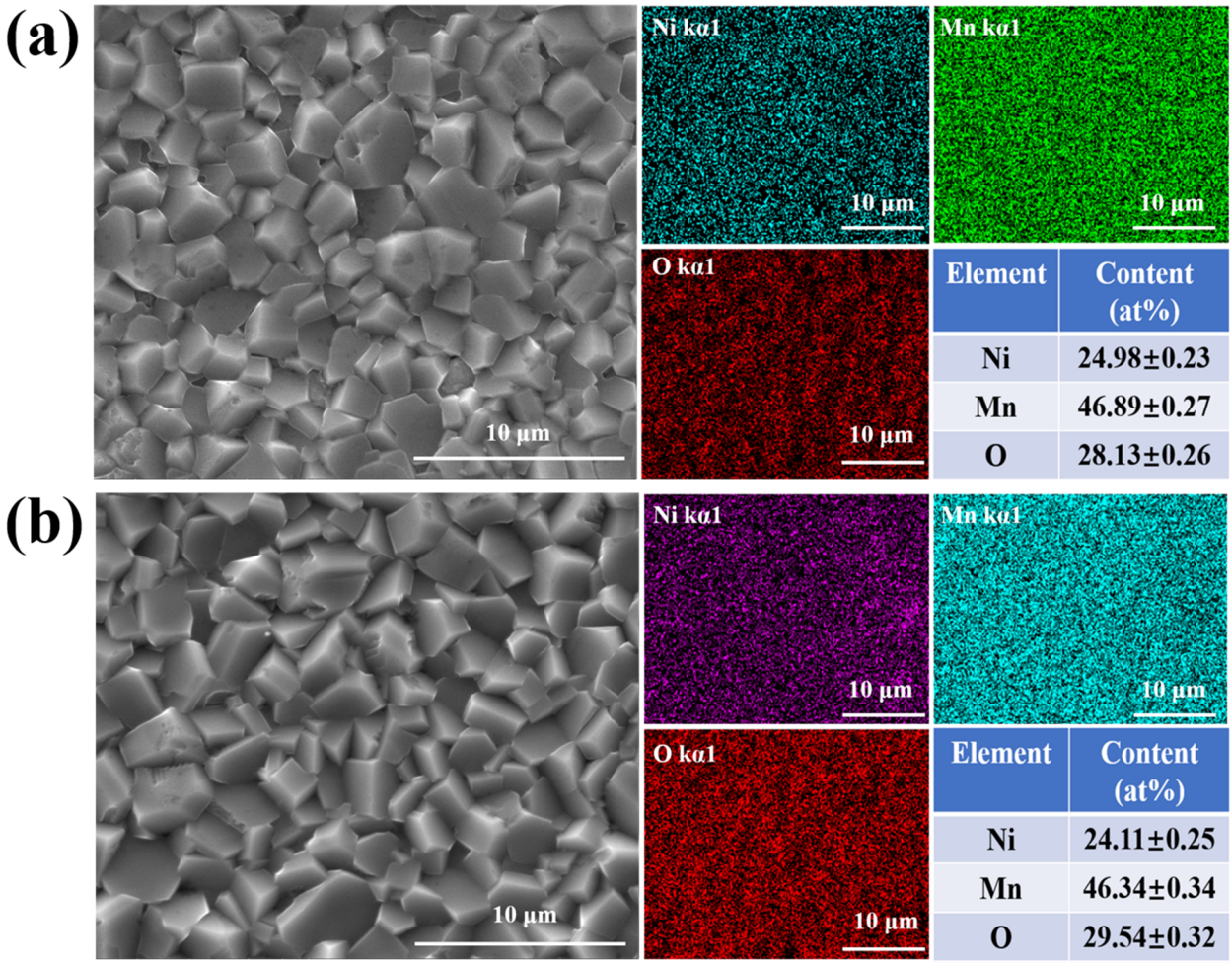

Element	Content (at%)
Ni	24.98±0.23
Mn	46.89±0.27
O	28.13±0.26

Element	Content (at%)
Ni	24.11±0.25
Mn	46.34±0.34
O	29.54±0.32

jace_17760_f4.tif

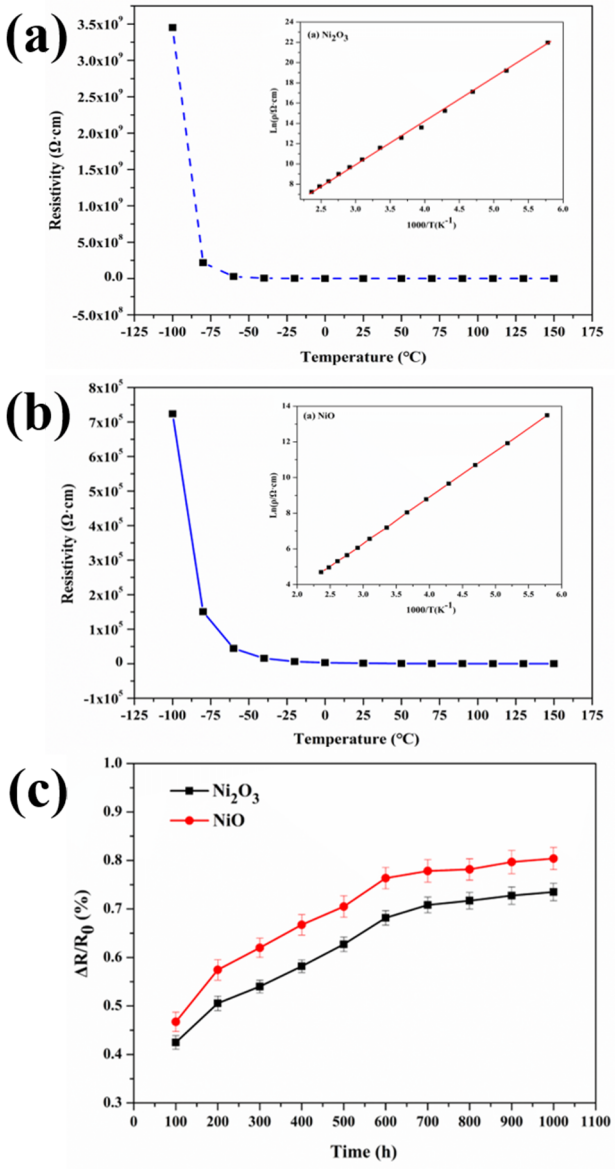

jace_17760_f5.tif

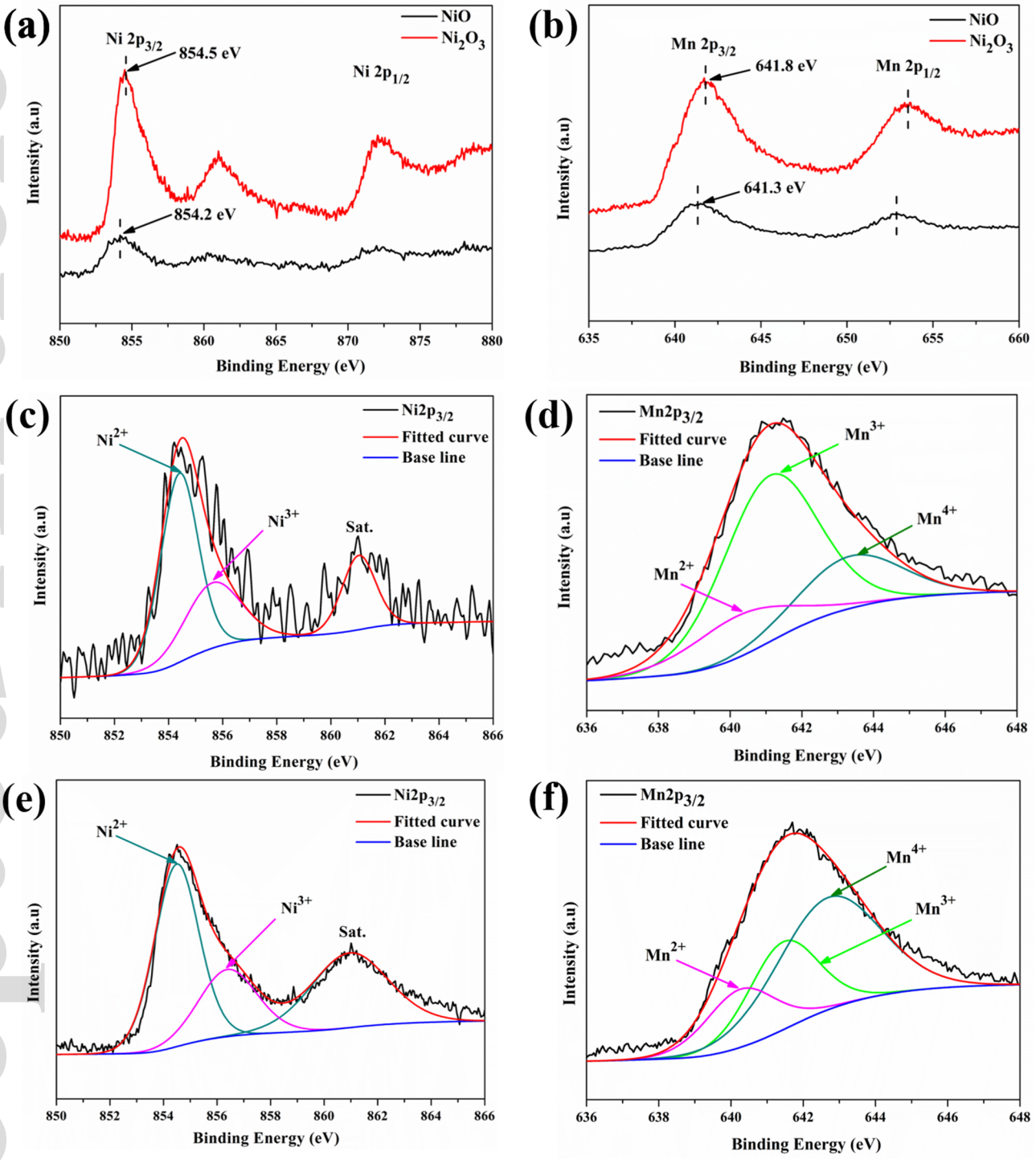

jace_17760_f6.tif

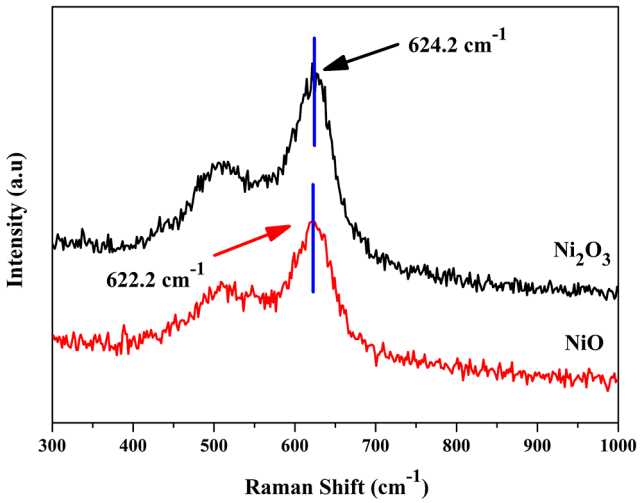

jace_17760_f7.tif